Solar Energy 280 (2024) 112872

Contents lists available at ScienceDirect

Solar Energy

journal homepage: www.elsevier.com/locate/solener

Exploring buried interface in all-vapor-deposited perovskite photovoltaics

Chun-Jen Shih [a], Yi-Sheng Chen [a], Dian Luo [a], Chang-Wei Yu [a], Kuan-Hung Chen [a], Galing Murokinas [a,b], Yu-Chen Huang [a], Chia-Feng Li [a,c], Yu-Ching Huang [a,c,d,*], Shun-Wei Liu [a,b,d,*]

[a] College of Engineering & Organic Electronics Research Center, Ming Chi University of Technology, New Taipei City 24301, Taiwan
[b] Department of Electronic Engineering, Ming Chi University of Technology, New Taipei City 24301, Taiwan
[c] Department of Materials Engineering, Ming Chi University of Technology, New Taipei City 24301, Taiwan
[d] Center for Sustainability and Energy Technologies, Chang Gung University, Taoyuan 33302, Taiwan

ARTICLE INFO

Keywords:
Perovskite
Vapor deposition
Buried interface
Photostability
Solar cell

ABSTRACT

All-vapor-deposited perovskite solar cells (PSCs) offer promising potential for maintaining high efficiency across large-area solar modules. However, a comprehensive understanding of device stability, particularly the crucial photodegradation mechanism under sunlight exposure, remains scarce in the existing literature. In this study, we investigate thermally co-evaporated perovskite polycrystals grown on two typical organic hole-transporting layers (HTLs), macrocyclic copper (II) phthalocyanine (CuPc) and the arylamine derivative of N4,N4,N4′,N4′-tetra([1,1′-biphenyl]-4-yl)-[1,1′:4′,1′-terphenyl]-4,4′-diamine (TaTm). Surprisingly, the robust CuPc limits the device performance with substantial non-radiative recombination loss and accelerates device degradation under light exposure. When built upon TaTm, the PSCs demonstrate a 47 times prolonged T_{80} lifetime (the efficiency drops to 80 % of the initial efficiency) of 1128 h by regulating the surface crystallography. By reducing the perovskite thickness to approach the buried heterojunction interface, we unravel the loss mechanism by directly observing crystallization dynamics. Our investigation reveals that surface polarity significantly influences the precursor adhesion, grain growth, and recombination dynamics at the HTL-perovskite interface. These findings underscore the critical role of the underlying surface in vapor-deposited PSCs, highlighting the potential for improved photostability through the regulation of interface imperfections.

1. Introduction

Among the emerging photovoltaic technologies, thin-film solar cells based on organic–inorganic hybrid lead halide perovskites, hereafter referred to as perovskites, stand out as the most promising material system [1]. The intense interest in perovskite stems from the unprecedented potential to obtain high-quality polycrystalline films through cost-effective deposition methods [2,3], ascribed to the low crystallization activation energy and high tolerance to constituent perturbation. Consequently, single-junction perovskite solar cells (PSCs) have experienced soaring growth within a mere decade of research development, achieving an exceptional power conversion efficiency (PCE) in the presence of high-density defect sites [4,5]. Despite holding great promises, the success of PSCs has so far been accomplished by the vast majority of literature focused on confined areas. Whether these laboratory-size perovskites are poised for feet-long solar modules with minimal efficiency loss remains challenging [6].

Thermal evaporation, a commercial physical vapor deposition practice for preparing organic light-emitting displays, is an alternative to developing large-area, homogeneous perovskites in a solvent-, contamination-free manner [7,8]. It sublimes solid-state compounds to the gaseous phase under high vacuum conditions before condensing on the substrates of interest. The ability of precise thickness control over consecutive stacking multilayers inspires single-junction PSCs with direct opposite polarity [9], tandem device structures [10], and flexible solar modules processed at low temperatures [11]. Unlike the predominant research based on accessible solution-based methods, a minor effort is devoted to advancing high-performance PSCs using thermally evaporated approaches [12,13]. A handful of vacuum-processed perovskites literature has been reported until recently [14,15], with encouraging photovoltaic performance comparable to the state-of-the-art PSCs [16]. However, these works took a prolonged layer-by-layer

* Corresponding authors at: College of Engineering & Organic Electronics Research Center, Ming Chi University of Technology, New Taipei City 24301, Taiwan.
E-mail addresses: huangyc@mail.mcut.edu.tw (Y.-C. Huang), swliu@mail.mcut.edu.tw (S.-W. Liu).

https://doi.org/10.1016/j.solener.2024.112872
Received 6 June 2024; Received in revised form 16 August 2024; Accepted 18 August 2024
Available online 24 August 2024

precursor deposition in sequence and were built upon solution-processed charge-transporting layers, further complicating the device fabrication procedure. In addition, despite the long-standing reputation of the solution-processed hole-transporting layers (HTLs) in delivering high-performance PSCs, they have become critical bottlenecks to fulfilling durable perovskite solar panels for a lifetime beyond decades [14,17].

Thermally evaporated charge-extraction layers guarantee low-efficiency losses for scaling up perovskite solar modules [18]. The promising industrial potential encourages the introduction of vacuum-processable organic molecules in PSCs. For example, small molecules such as N4,N4,N4′,N4′-tetra([1,1′-biphenyl]-4-yl)-[1,1′:4′,1′-terphenyl]-4,4′-diamine (TaTm), an arylamine derivative, has been recurrently utilized as HTL in high-performance PSCs with an inverted *p-i-n* structure [9,12,19]. The long π-conjugation of TaTm supports electron-resonance stabilization, which should achieve small reorganization energy and promote the probability of the electron-hopping process (favors hole mobility in this case). Another common HTL is metal phthalocyanine, a class of macrocyclic molecules renowned for their high carrier mobility, suitable energy level, and chemical stability [20]. In particular, copper (II) phthalocyanine (CuPc) was employed by Tavakoli et al. as a dopant-free hole-selective contact for fully evaporated PSC with negligible hysteresis [21]. Johnston et al. demonstrated the thermal stability of CuPc restricted the device degradation, with no degradation found after 3710 h of continuously stressing the device at 85 ℃ [22]. In addition, Xu et al. chose CuPc in favor of the conformal coating perovskite precursor solution on textured substrates for perovskite/silicon tandem configuration [23]. However, this information differs from the empirical findings that Paetzold et al. gathered from thermally co-evaporated perovskite [24], suggesting that a non-polar surface is critical in incorporating organic compounds into the perovskite framework. Whether the robust yet hydrophilic CuPc is an ideal HTL for all-vapor-deposited PSCs remains controversial. While tremendous improvements have been made to advance operational stability over the last decade of research focus, most of the knowledge was gained from solution-based treatment [25]. Stranks et al. found that the thermal and ambient air stability of vapor-deposited perovskite was remarkably improved with the inclusion of excess PbI_2 [26]. However, the device dropped 10 % of the initial performance after only 35 h of continuous operation, which can be attributed to the nature of PbI_2 photolysis and solution-processed HTL. A shortage of insight into the photostability of the vacuum-deposited PSCs was found in the literature, particularly the buried interface beneath the thermally evaporated perovskite [27,28].

In this work, we focus on exploring cost-effective and durable HTLs for single-junction wide-bandgap PSCs. As opposed to the prolonged period of the layer-by-layer deposition for perovskite generation, we deposit the $FA_{0.9}Cs_{0.1}Pb(I_{0.9}Br_{0.1})_3$ perovskite layer via a ternary co-sublimation process in favor of throughput requirement for industrialization [29]. The all-vapor-deposited *p-i-n* PSCs show maximum PCEs of 11.71 % and 15.57 % for CuPc and TaTm-based devices, respectively. To our surprise, the CuPc-based device loses 20 % of its initial PCE value (T_{80} lifetime) in 24 h against successive light soaking conditions, where it takes more than 47 days for TaTm-based PSC to decay to the same level. Despite a greater extent of non-radiative recombination of the CuPc-based PSC, identified in electroluminescence (EL) and photoluminescent (PL) analysis, it is challenging to investigate the buried HTL-perovskite interface with scanning electron microscopy (SEM) images. In this case, we systematically explore the interfacial losses by examining the surface morphology of vapor-deposited perovskite precisely close to the contact via atomic force microscopy (AFM). It is advised that the adhesive behavior of FAI precursor has profound consequences in perovskite formation in the vicinity of the HTL-perovskite interface, and the substrate polarity plays a pivotal role in regulating the localized perovskite crystallography from the nano-scale scope and, eventually, the overall device longevity. We believe the interaction between substrate surface and vapor-deposited perovskite found in this work is not limited to vacuum-processed *p*-type HTLs but applies to other device architectures, such as the *n-i-p* configuration or more complicated tandem stacks.

2. Material and methods

2.1. Crude material

The materials, including TaTm, CuPc, and 2,9-Dimethyl-4,7-diphenyl-1,10-phenanthroline (BCP), were acquired from Shine Materials. The fullerene (C_{60}) was purchased from 1-Material. MoO_3 and perovskite precursors, including PbI_2 (99.9985 % metal basis) and CsBr (99.999 % metals basis), were provided by Thermo Scientific Chemicals. The formamidinium iodide (>99.99 %) and formamidinium bromide (>99.99 %) were purchased from Greatcell Solar. MeO-2PACz was purchased from Tokyo Chemical Industry Co., Ltd.. N, N-dimethylformamide (DMF) and dimethyl sulfoxide (DMSO) were obtained from Acros Organics. Ethyl acetate was purchased from Fisher Chemical. All materials were used as received. The ITO-coated glass substrates were purchased from Lumtec Corporation, whereas the FTO-coated substrates were purchased from FrontMaterials. Before thin film deposition, the substrates were cleaned with diluted detergent, deionized water, acetone, and isopropanol in a sonication bath for 10 min each.

2.2. All-vapor-deposited perovskite solar cells

The ITO-coated substrates were loaded into the thermal evaporation chamber (Syskey Technology). A 10^{-6} torr base vacuum level was guaranteed before thin film deposition. After that, a 6 nm of non-stoichiometric MoO_3 was first deposited to ensure ohmic contact with the anode, followed by the hole-transporting layer deposition (CuPc 10 nm, TaTm 10 nm, or CuPc 10 nm/ TaTm 10 nm). We fixed a total thickness of 20 nm for the CuPc/TaTm bilayer to keep the same recipe of individual layers as that of CuPc- and TaTm-based PSCs. The samples were transferred to a second chamber for perovskite thin film deposition. The co-evaporation process was performed with a 0.15, 0.8, and 1.1–1.2 Å/s deposition rate for CsBr, FAI, and PbI_2, respectively. The perovskite thin films changed to a dark brownish after post-annealing treatment (135 ℃ for 30 mins) in an N_2-filled glovebox (MBraun). The perovskite solar cells were finalized after the successive deposition of C_{60} (10 nm)/BCP (7 nm)/Ag (100 nm) multilayer structure. An energy level diagram has been included in the Supporting Information (Fig S1). The actual thickness of each layer was calibrated with a surface profiler (Bruker, DektakXT). The active area of the device was 4 mm^2. To characterize the photovoltaic performance in the ambient atmosphere that conforms to the ISOS-L-1 standard, we transferred the perovskite devices to the N_2-filled glovebox (O_2 < 0.1 ppm; H_2O<0.1 ppm) for encapsulation. Note we chose a glass-to-glass encapsulation sealed with UV-curable epoxy resin (Everwide Chemical Corporation Limited EXC345) to prevent air ingress. A more practical approach would require a commercial encapsulation technique that passes the damp heat test for outdoor testing.

2.3. Solution-processed perovskite preparation

The MeO-2PACz HTL layer (0.3 mg/mL in ethanol) was spin-coated onto the clean FTO-coated substrate (see cleaning protocol above) at 3000 rpm for 30 s, following post-annealing treatment at 100 ℃ for 10 mins in air. A 1.4 M perovskite precursor solution was prepared by mixing CsI, FAI, FABr, and PbI_2 in the DMF and DMSO mixture (4:1, v/v; 1 mL). This solution was then spin-coated onto the as-prepared HTL film at 5000 rpm for 30 s in a glove box filled with N_2. After spinning for 20 s, 300 μl of ethyl acetate antisolvent was dropped on the sample, forming a transparent intermediate perovskite phase. The samples were then annealed on a hot plate (first at 150 ℃ for 10 mins and then at 100 ℃ for 2 mins) to form the dark-brown perovskite films.

2.4. Characterization

All measurements were performed in an ambient atmosphere (room temperature ~25 ℃; relative humidity ~65 %). The photovoltaic performance was evaluated under the AM1.5G one sun solar simulator (Enlitech, SS-X). The external quantum efficiency (EQE) spectrum and the corresponding integrated current density were measured using a quantum efficiency measurement system (Enlitech, QE-R) recorded in AC mode with the calibration in advance (Hamamatsu S1337). The V_{oc}-loss Analyzer (Enlitech, REPS) recorded the electroluminescence spectrum and quantum efficiency. The photostability of the perovskite solar cells was evaluated by soaking the device with one sun equivalent intensity of a white LED source (Newport, LSH-7320). The light intensity was periodically checked with a silicon reference cell. The absorption spectra were recorded by the UV–Vis spectrometer (Jasco, V-770), while the photoluminescence spectrum was recorded by the spectrofluorometer (HORIBA, FluoroMax Plus). The spectrometer (Edinburgh, FLS1000) recorded the transient photoluminescence dynamics with a pulse laser of 447 nm. The laser was operated at a 500 ns excitation duration. The X-ray diffraction pattern was recorded with an X-ray analyzer (Bruker, D2 PHASER). The scanning electron microscopy images and the elemental analysis were captured with an ultra-high resolution field emission microscope (Hitachi SU8200) operating at an accelerating voltage of 3 kV over platinum metalized samples. The grazing incidence wide-angle X-ray scattering patterns were recorded at the 23A beamline station (National Synchrotron Radiation Research Center, Taiwan), with analysis following the previous report [29]. The surface morphology images were captured by atomic force microscopy

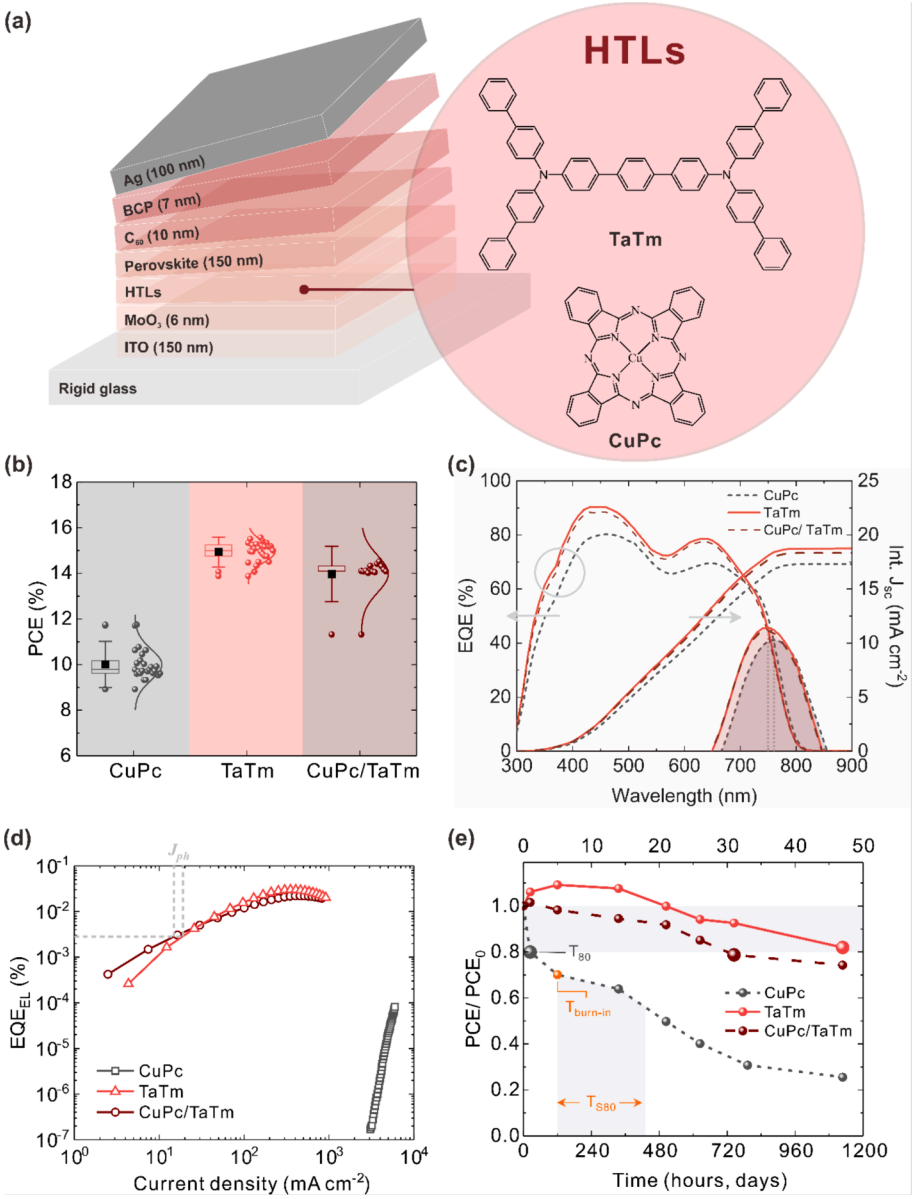

Fig. 1. Photovoltaic performance of the all-vapor-deposited PSCs. (a) The schematic illustration of the fully evaporated *p-i-n* PSCs built upon different organic HTLs with insets of the molecule structure. (b) The PCE distribution of the devices based on CuPc, TaTm, and CuPc/TaTm HTLs. (c) The EQE spectrum for the champion devices and the corresponding integrated J_{sc}. The derivative of the EQE spectrum edge is shaded (arbitrary unit). The circle highlights the slope change around the wavelength of 370 nm. (d) The EQE_{EL} characteristics with respect to various injection current densities under dark conditions. The photocurrent (J_{ph}) is as labeled. (e) The degradation dynamic of the devices under continuous one-sun equivalent soaking (ISOS-L-1 standard). The shaded area shows the 100–80 % region from the initial performance. An alternative estimation (T_{S80}) is given for the CuPc-based PSC after the initial burn-in (shown in orange). (For interpretation of the references to colour in this figure legend, the reader is referred to the web version of this article.)

(Bruker, Innova).

3. Results and discussion

3.1. Device performance

We simultaneously sublimate formamidinium iodide (FAI), lead iodide (PbI_2), and lead bromide (CsBr) precursors to form the perovskite active layer (see Material and methods). Although multi-ion composition thermodynamically stabilizes black-phase FA-based perovskite at room temperature, we introduced rather restricted CsBr content to prevent halide segregation under light exposure or bulk recombination attributed to irregular morphology [30,31]. Note that we have screened the perovskite composition by varying the precursor rate on individual substrate surfaces, and optimal photovoltaic performance is received with a 5 % excess PbI_2 from the stoichiometric case (assured with energy-dispersive X-ray spectroscopy), a balance of defect passivation without compromising charge extraction [26,32]. The all-vapor-deposited PSCs were constructed by developing a perovskite layer on the substrate decorated with different intrinsic organic HTLs (CuPc and TaTm) in the *p-i-n* stacking configuration, respectively (Fig. 1a). These two candidates have been widely utilized in the literature without additional dopants because of their high mobility and share the highest occupied molecular orbital (HOMO) level in accord with the photoactive perovskite layer. The PCE distribution of 25 individual devices under AM 1.5G solar illumination is recorded for CuPc, TaTm, and CuPc/TaTm bilayer structures (Fig. 1b), respectively. When the perovskite is developed on TaTm HTL, the PSC presents an open-circuit voltage (V_{oc}) of 1.05 V, a short-circuit current density (J_{sc}) of 19.25 mA cm^{-2}, a fill factor (FF) of 77.05 %, and a PCE as high as 15.57 %, which is comparable to the previous studies with similar composition given a 150 nm perovskite layer constructed [32]. For the CuPc-based PSCs, the device performance demonstrates a V_{oc} of 0.94 V, a J_{sc} of 15.08 mA cm^{-2}, and an FF of 71.01 %, counting for a PCE of 9.7 %. Compared to the TaTm-based PSCs, the CuPc HTL device demonstrates a more extensive spread in all three metrics describing photovoltaic performance (Fig. S2). Specifically, a substantial V_{oc} drop of more than 100 mV observed from the perovskite built upon CuPc highlights the different charge carrier mechanisms between the two devices. Although we expected the CuPc/TaTm bilayer to unleash the power of CuPc (photostability and hole-extraction ability) and TaTm (electron-blocking ability and hydrophobicity), the CuPc/TaTm-based device still suffers slight non-radiative recombination losses (Fig. S2). Further modification may suppress the non-radiative recombination while supporting an efficient hole extraction. We recorded the external quantum efficiency (EQE) of the champion devices to various monochromatic lights and the corresponding integrated J_{sc} value in Fig. 1c. All devices show a clear efficiency drop beyond the wavelength of 550 nm. Although this can be ascribed to the transmittance loss for the devices that include a CuPc layer (Fig. S3), we attribute this behavior to the mismatched distribution of the optical field and charge generation, as well as the enhanced reflection loss of a thin perovskite layer that was constructed [33]. Additionally, a slope change can be observed for the TaTm-based device at the wavelength of 370 nm (marked in Fig. 1c), which can be aroused by the characteristics of the TaTm layer (Fig. S3). To estimate the bandgap energy of the PSC, we take the inflection point of the spectra derivative (∂EQE/ ∂E). The bandgap is around 1.65 eV with a slightly bathochromic shift for the perovskite constructed on CuPc. We believe this can be ascribed to the surface polarity that favors FAI aggregation, which will be elaborated later on. Nonetheless, the TaTm-based PSC can utilize most of the visible photons, while a general efficiency loss is found on CuPc-based PSCs in line with the J_{sc} characteristic obtained from Fig. S2b.

To study the V_{oc} loss aroused by the interface, we characterize the external quantum efficiency of the radiative electroluminescence (EQE_{EL}) from the PSCs in the dark (Fig. 1d). Generally, a higher EQE_{EL} stems from radiative relaxation from the injected current instead of recombination loss via non-radiative pathways based on the equation of [34]:

$$V_{oc} = \frac{k_B T}{e} \ln\left(EQE_{EL} \frac{J_{ph}}{J_{em}} + 1 \right) \quad (1)$$

where k_B is the Boltzmann constant, T is room temperature in our case, e is the elementary charge, J_{ph} represents the current under light illumination, and J_{em} stands for the current of absorbed/emitted photon flux in equilibrium aroused by the thermal radiation from the surrounding. As a result, the V_{oc} deficit induced by the non-radiative recombination can be assessed according to:

$$V_{loss}^{non-rad} = -\frac{k_B T}{e} ln EQE_{EL} \quad (2)$$

A close EQE_{EL} value between TaTm and CuPc/TaTm-based PSCs with a deduced non-radiative V_{oc} loss of 260 mV is obtained, close to the value obtained from thermally evaporated inorganic PSCs [35]. However, a stark contrast is observed on CuPc-based PSCs with a limited radiative intensity. Note that although one should calculate the loss at the recombination current density equal to the J_{sc} under one-sun solar illumination, we cannot collect helpful information from the CuPc-based device at this level due to its low radiative intensity. Nevertheless, the above quantitative analysis suggests a substantial non-radiative recombination loss at the CuPc-perovskite interface, which can be suppressed once TaTm is inserted at this heterojunction interface.

A consensus has emerged on vacancy-assisted halide redistribution acting as the degradation pathway under light illumination with activation energy as low as 0.6 eV [36]. It has been proposed that chemically neutralizing the mobile defects or the decoration of low-dimensional perovskite can curb halide-driven decomposition [37,38]. However, a lack of photostability assessment was found from all-vapor-deposited PSCs, let alone a facile strategy developed for the in-vacuum fabrication. Here, we evaluate the intrinsic device photostability by following the protocols based on the International Summit on Organic Photovoltaic Stability (ISOS) [39]. The assessment was performed with one-sun equivalent illumination under ambient conditions, conforming to the ISOS-L-1 standard. Note that we chose a typical glass-to-glass sealing to prevent moisture ingress that stimulates the hygroscopic nature of organic cation. As shown in Fig. 1e, the CuPc-based PSCs experienced a monotonic decay after the initial rapid drop (often termed "burn-in"). It took only 24 h of continuous one-sun exposure for the device to lose 20 % of the initial performance (T_{80}), that an extended lifetime of 310 h (denoted as T_{S80}), during which the PCE dropped 20 % of its magnitude after the end of the burn-in process ($T_{burn\text{-}in}$), can be extrapolated. Although it usually takes rapid progress for the initial burn-in followed by a stabilized degradation profile, this behavior should be prohibited to guarantee maximum performance of the PSCs. Intriguingly, it has been validated the burn-in behavior should be ascribed to the pattern of cation migration on a timescale of several hours under illumination with a direct trace of compositional redistribution over the entire PSC [40,41]. Namely, instead of the most vulnerable halide migration under lighting, a cation redistribution could be the reason for the burn-in feature observed on our all-vapor-deposited PSCs consisting of CuPc HTL (with a significant loss on J_{sc} over time in Fig. S4). However, TaTm-based PSCs followed a non-monotonic degradation without the appearance of initial burin-in behavior, achieving a T_{80} lifetime beyond 1,128 h (~47 days). To our knowledge, this photostability is one of the best-performing vapor-deposited PSCs to date (see Table 1) [42]. It indicates the critical character of the underlying charge transporting layer (HTL in our case) for the device longevity as a whole and requires in-depth insight into the efficiency loss in the CuPc-based case, given the robustness of the CuPc molecule itself.

Table 1
Summarized information on the thermally evaporated perovskite solar cells that includes a photostability assessment.

Protocols[a]	Light source[b]	Condition[c]	Load[d]	Encapsulate	Lifetime (hours)[e]	Reference
ISOS-L-1I	Candlelight LED	N_2	MPP	No	T_{90} ~ 120	[9]
ISOS-L-1	NA	Ambient	MPP	Yes	T_{90} = 35	[32]
ISOS-L-1I	White LED	N_2	OC	No	T_{90} = 100	[21]
ISOS-L-1I	NA	N_2	OC	NA	T_{80} = 500	[11]
ISOS-L-1I	Candlelight LED	N_2	MPP	Yes	T_{90} = 340	[12]
ISOS-L-1I	Candlelight LED	N_2	MPP	Yes	T_{90} = 720	[42]
ISOS-L-1	White LED	Ambient	MPP	Yes	T_{90} ~ 60	[45]
ISOS-L-1I	Candlelight LED	N_2	MPP	Yes	T_{80} = 495	[54]
ISOS-L-1I	White LED	N_2	MPP	No	T_{92} = 450	[16]
ISOS-L-1I	White LED	N_2	OC	No	T_{92} = 528	[15]
ISOS-L-1	Newport (LSH-7320)	Ambient	OC	Yes	T_{80} = 1,128 T_{90} = 830	This work

[a] The protocols developed by the International Summit on Organic PV Stability (ISOS).
[b] The light source employed as the aging stressor. It should be noted that the spectrum and detailed information of the light source are not available in the previous literature, which can undermine the reliability of the assessment [42].
[c] The measurement environment is either in an ambient atmosphere or a nitrogen-filled glovebox.
[d] OC stands for open-circuit condition, whereas MPP represents maximum power point tracking.
[e] The time for the device to decay 10% (T_{90}) or 20% (T_{80}) from the initial performance.

3.2. Photophysical properties

To avoid the pitfalls of EL characterization from complete PSCs, with imbalanced charge transport and require current density higher than J_{sc} for samples that prefer non-radiative recombination [43], we analyze the half-stack configuration of ITO/ MoO_3/ HTLs (CuPc, TaTm, and CuPc/ TaTm)/ perovskite in the following sections. The absorbance spectra of the perovskite fabricated on individual HTLs are shown in Fig. 2a. All thin films share the absorption profile with an onset wavelength of around 775 nm in high similarity, with a deduced bandgap of 1.6 eV from the corresponding Tauc plot. The typical bandgap offset between the absorption onset and the EQE spectrum (1.65 eV in Fig. 1c) can originate from the energy-dependent recombination rates [44]. Nonetheless, both bandgaps advise that limited bromide is incorporated into the perovskite solid. [12,22]. This guarantees confined halide segregation of the perovskite into different domains. Indeed, we find no other transition bands or components but a single representative PL spectra from all samples in Fig. 2b, validating a phase-pure perovskite formation. However, a different intensity is found when the perovskite is deposited on different HTLs. While comparable intensities are found between the perovskites deposited on TaTm and CuPc/TaTm, a suppressed PL spectrum is recorded on the CuPc-based perovskite. We

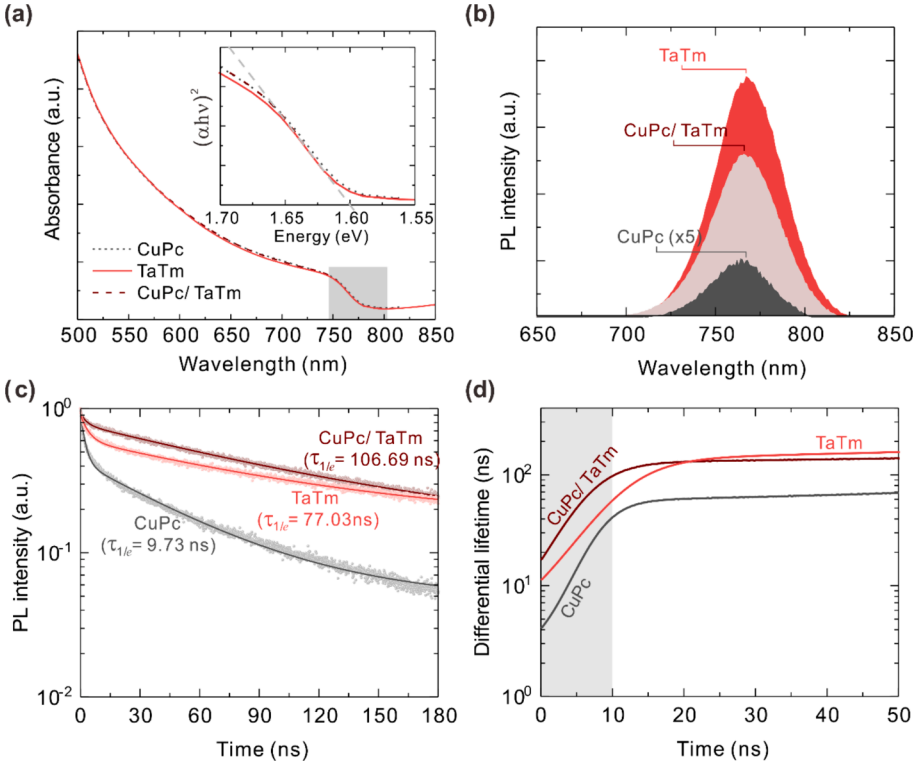

Fig. 2. Photophysic study of the perovskite thin film deposited on different organic HTLs. (a) The UV–Vis absorption spectra. The inset shows the corresponding Tauc plot for bandgap estimation. (b) The unnormalized PL spectra from an excitation wavelength of 320 nm. Note that the intensity of the perovskite deposited on CuPc is magnified by a factor of 5 for observation. (c) Time-resolved photoluminescence (TRPL) from a pulse laser source of 447 nm. The decay profiles are reproduced with double exponential approximation ($y = A_1 \exp(-x/t_1) + A_2 \exp(-x/t_2) + y_0$). (d) The differential lifetime $\tau_{diff}(t) = -(d\ln\Phi(t))/dt)^{-1}$ deduced from (c), where the initial ten nanoseconds are shaded.

believe this is attributed to the different levels of non-radiative recombination given the EL results from Fig. 1d. This highlights substantial non-radiative recombination density from the CuPc-perovskite interface, insinuating an unfavorable scenario against perovskite formation at the contact. To explore the underlying causes governing the charge transfer dynamic at the contact, we track the transient PL decay with a double exponential approximation in Fig. 2c, which reflects the different behavior of the charge carrier recombination processes [22]. In particular, the monoexponential decay at delayed time gives information about the non-radiative recombination that can be readily described by the Shockley-Read-Hall model [45]. The perovskite thin film based on TaTm follows a slower decay with a longer time constant $\tau_{1/e}$ (defined as the time drops to $1/e$ of the initial intensity) than that based on CuPc. We further estimate the differential lifetimes (Fig. 2d) by finding the derivative of the PL profile. Compared to the device based on TaTm, the CuPc and CuPc/TaTm samples show a rapid transition around 10 ns, signifying a faster carrier extraction from the interface [19]. We believe the high mobility of CuPc expedited the hole extraction of CuPc/TaTm-based perovskite with the most prolonged transient PL decay in Fig. 2c. The steadily increased lifetime at the early time can be ascribed to the radiative recombination of the perovskite, while the differential lifetime saturates at a constant value at a longer time scale dominated by non-radiative recombination [22]. The lower differential lifetime of the perovskite deposited on CuPc indicates higher trap-assisted recombination at the CuPc-perovskite interface compared to the perovskite constructed on TaTm or CuPc/ TaTm surface, which matches well with the information received from EL characterization (Fig. 1d).

3.3. Crystallographic studies

We investigate the crystalline properties of the perovskite deposited on different HTLs with the XRD pattern shown in Fig. 3a. A typical signature of black α-phase perovskite and the crystalline PbI_2 can be observed with no event of yellow δ-phase $FAPbI_3$ or $CsPbI_3$ inclusions in the profile. The clear PbI_2 signal (5 % excess PbI_2 evaporation rate) is comparable to the representative (1 1 0) perovskite and relatively weak compared to the results presented by Stranks et al. with much more PbI_2 [26]. Compared to the perovskite deposited on CuPc, a stronger representative intensity of {1 0 0} planes is observed when deposited on the TaTm or CuPc/ TaTm bilayer. It should be noted that the appearance of (1 1 0) and (2 1 0) characters signifies the formation of alternative crystal orientations [22]. Nevertheless, these signals can be suppressed when the perovskite is deposited on TaTm. In fact, the Grazing Incidence Wide-Angle X-ray Scattering (GIWAXS) characterization advises a preferential ordering of perovskite films constructed on TaTm (Fig. S5). By directly juxtaposing the 2D GIWAXS patterns of the perovskite polycrystal deposited by either vapor deposition or solution process, a high degree of structural orientation is discovered on vapor-deposited thin film as opposed to the diverged crystallization of the solution-based perovskite with multiple diffraction rings. This implies the unique crystallographic features of the vapor-deposited perovskite with an anisotropic nature [46], which will be elaborated in the following section. Meanwhile, the SEM images of the half-stack device are captured for direct crystal identification (Fig. 3b-d). Despite deliberately choosing a stoichiometric-excess PbI_2 for passivation, it leaves no trace of observable entities in top-view images but well-defined grain-to-grain crystalline boundaries [26]. Although the vapor-deposited perovskite follows a somewhat limited coalescence process for large grain

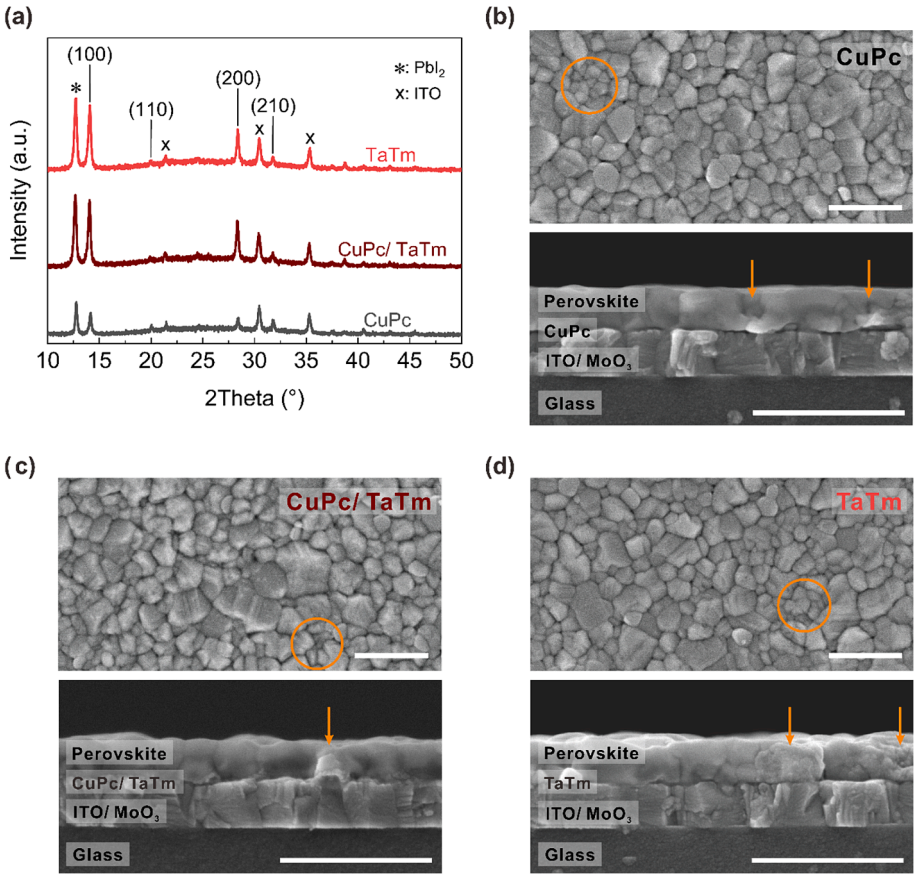

Fig. 3. The crystalline properties of perovskite built atop different HTLs. (a) The XRD patterns of the half-stack devices. The peaks corresponding to PbI_2 and ITO are labeled. (b–d) The top view and cross-sectional SEM images of the half-stack devices. Distorted regions are highlighted. Scale bar: 500 nm.

formation, accounting for a grain size of 100–200 nm in typical cases, we observe clear crystal planes in larger entities in our thin film, which signifies the quality of perovskite crystal deposited on organic HTLs. Moreover, we find that the grain size distribution of perovskite when deposited on the TaTm is more homogeneous than that fabricated on CuPc. Indeed, a slightly narrow full width at half maximum of the EL spectrum suggests a higher homogeneity of perovskite grain constructed in TaTm-based PSC (Fig. S6) [47]. The cross-sectional SEM images elucidate the broad picture of morphology change that pervades throughout the solid. As shown in Fig. 3, all vapor-deposited perovskite keeps a close-packed formation attached to the contact interface, with preferential cuboid grain growth normal to the substrate over horizontal homogenization. However, distorted morphologies are distributed above the area where phase segregation appears in CuPc and CuPc/TaTm-based half-stack. The compositional inhomogeneous can lead to energetic misalignment at the contact [48,49]. Also, a localized distorted morphology of granular grains comes in clusters that can be observed on the TaTm-based perovskite. Overall, although the vapor-deposited perovskite polycrystal presents a small grain size on average, the highly oriented crystallography should, in principle, form a homogeneous surface with fewer facets exposed to the following adjacent layer. This could inhibit interfacial recombination at the surface atop for charge extraction with limited dangling bonds [50]. In addition, the findings presented so far emphasize the importance of the contact surface beneath the perovskite, where this interface affects not only the initial nucleation stage but also the crystallization process onwards. We believe a more profound analysis is required to explore the crystal morphology from a closer scale.

3.4. Buried interface of vapor-deposited perovskite

While various reports indicate that the substrate beneath could profoundly affect the crystallography of vapor-deposited perovskite, an empirical discussion was delivered until Abzieher et al. examined the perovskite crystallization dynamic on a wide range of substrate materials [24]. However, instead of the disparate orientation of methylammonium-based perovskite deposited on the non-polar surfaces, with preferential crystal growth perpendicular to the {1 1 0} and {1 1 1} planes, we find an anisotropic nature of highly preferred {1 0 0} orientation in our case, especially the perovskite constructed on TaTm (Fig. 3a). Here, we explore the nucleation and crystallization dynamics of vapor-deposited perovskite by directly observing perovskite formation in Fig. 4. Unlike the in-situ characterization of the molecule behavior at the interface or through a facile lift-off strategy [51,52], we

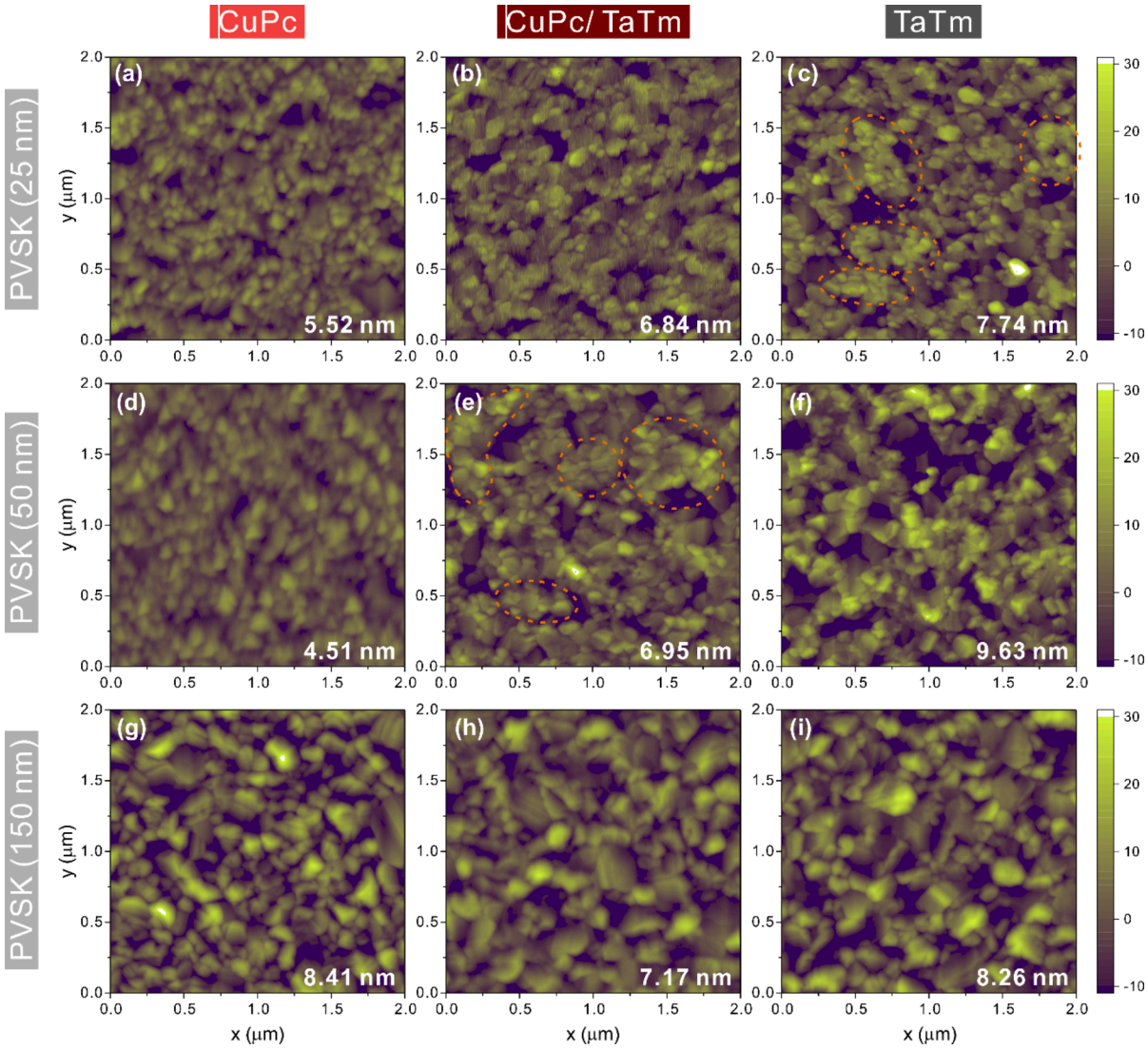

Fig. 4. AFM images of the perovskite dynamics. (a–c) The initial perovskite formation on different HTLs. Clusters are labeled in dash lines. (d–f) The thin perovskite layer built upon different HTLs. (g–i) The final perovskite layer built upon different HTLs. The root mean square value of the surface roughness is labeled. Note all samples were annealed before characterization.

examine the surface morphology of perovskite polycrystal approaching the buried interface with AFM characterization. Although reducing the bulk thickness may create a condition that deviates from the actual scenario, given the gradient distribution of the in-plane strain component normal to the substrate [53], we deliver a general concept that the underlying material dictates the perovskite growth from the interface. At the initial stage of the perovskite formation (Fig. 4a–c), a high nucleation site density is distributed throughout the surface. In contrast to the high coverage over the CuPc-based substrate with low root mean square value, clusters of independent nuclei are formed on the TaTm substrate through aggregation (as highlighted in Fig. 4c). This thermodynamically stable morphology is sustained until the critical thickness of the coalescence process takes place (Fig. 4f). The small nuclei first collapse and unify into larger crystallites, as evidenced by the increased grain size and surface roughness. This is similar to the previous work and can be described as the Ostwald ripening process [21]. However, the small grains on the CuPc failed to initiate the crystallization process at the perovskite thickness of 50 nm (Fig. 4d), but an even higher substrate coverage is found with the lowest roughness. Actually, this behavior can be suppressed after the insertion of TaTm at the CuPc-perovskite interface (Fig. 4e), albeit with a smaller average grain size than that without CuPc (Fig. 4f). Namely, it is clear that a large amount of unreacted nuclei is dispersed at a thickness of up to 50 nm built on top of CuPc (Fig. 4d), contrasting with that observed on CuPc/TaTm (Fig. 4e) or TaTm (Fig. 4f). We believe the delayed crystallization process of the perovskite built upon CuPc not only leaves a high density of unreacted aggregates at the buried interface, deteriorating charge collection with recombination events [54], but strongly insinuates the malignant interface responsible for device longevity. Note that the buried topography can hardly be distinguished from the perovskite with a thickness up to 150 nm (Fig. 4g–i), which resembles that observed from SEM images (Fig. 3). Although it usually takes a perovskite thickness beyond 500 nm to exploit sunlight for current generation fully, this would put more than three times the deposition load on the fabrication process compared to the perovskite constructed in this work. We believe the finding here applies to solar cells with thicker active layers. We explore the surface chemistry between the substrates to unravel the reason behind this phenomenon. The AFM images of the HTL and the HTL covered with FAI are provided in Supporting Information (Figs. S7 and S8). It has been suggested that substrate polarity is the driving force for precursor adhesive behavior, directly influencing the preferable crystal growth [22,24]. Indeed, the CuPc thin film shows a hydrophilic attribute that changes the adhesive behavior of the organic precursor on the substrate (Fig. S8d). The large sticking force between FAI molecules creates a non-uniform distribution of precursor framework, which prohibits perovskite crystallization with a significant fluctuation in the event of precursor reaction.We prepared the device based on another hydrophobic HTL, 2,2′,7,7′-tetra(N,N-di-p-tolyl)amino-9,9-spirobi-fluorene (Spiro-TTB) to verify the findings. The photovoltaic performance of the device based on Spiro-TTB is included in the Supporting Information (Table S1). Overall, an understanding of the mechanism that guides the perovskite crystallization has been elucidated by examining the topography in the vicinity of the surface beneath through nano-scale observation. The information given here goes beyond the previous study that focuses on the influence of the substrate material on the perovskite composition and electronic structure but points out that the initial perovskite formation at the buried interface can have a critical impact on the device longevity. Note that the evidence presented thus far supports the idea that a non-polar surface promotes vapor-deposited perovskite at the initial stage of crystallization, which contrasts with the knowledge gained from solution-processed perovskite. Further passivation of the perovskite top surface may lead to durable PSC towards commercialization [55,56,57].

4. Conclusions

Our investigation focused on elucidating the photostability of all-vapor-deposited wide-bandgap PSCs. As the pursuit of stability in next-generation photovoltaics necessitates robust interfacial layers that are chemically stable and resilient to various stressors over extended device operation periods, we have observed significant variations in device durability despite the inherent stability of the HTL molecule itself. Our findings indicate that the choice of HTL material influences the durability of the PSCs. Specifically, when the perovskite layer was deposited on the CuPc HTL, the T_{80} lifetime of the device was merely 24 h, whereas the T_{80} lifetime reaches over 1128 h (~47 days) in the TaTm-based PSC. Insights gleaned from EL and PL analyses have pointed to a substantial degree of non-radiative recombination loss at the CuPc-perovskite interface. We reduced the perovskite thickness to investigate this phenomenon further, which is governed by the concealed interface. Despite similar macroscopic morphology in the perovskite bulk, a different behavior was observed when probing the crystallization dynamics at the nano-scale level near the HTL-perovskite interface. The presence of high-density imperfections serves as non-radiative recombination centers responsible for the photodegradation process. Our study revealed that substrate polarity beneath the perovskite is pivotal in driving vertical heterogeneity within the vapor-deposited perovskite. We posit that the interaction between surface polarity and perovskite formation, as uncovered in this study, transcends the specific context of thermally evaporated PSCs. Rather, it likely extends to other methodologies processed under high vacuum conditions, such as chemical vapor deposition, magnetron sputtering, pulsed laser deposition, and close-space sublimation.

CRediT authorship contribution statement

Chun-Jen Shih: Writing – original draft, Visualization, Methodology, Investigation, Formal analysis, Conceptualization. **Yi-Sheng Chen:** Project administration, Formal analysis, Data curation. **Dian Luo:** Investigation, Formal analysis. **Chang-Wei Yu:** Validation, Investigation. **Kuan-Hung Chen:** Validation, Investigation. **Galing Murokinas:** Validation, Investigation. **Yu-Chen Huang:** Writing – review & editing, Supervision, Resources, Funding acquisition. **Chia-Feng Li:** Investigation. **Yu-Ching Huang:** Writing – review & editing, Supervision, Resources, Funding acquisition. **Shun-Wei Liu:** Writing – review & editing, Supervision, Resources, Funding acquisition.

Declaration of competing interest

The authors declare that they have no known competing financial interests or personal relationships that could have appeared to influence the work reported in this paper.

Acknowledgements

The authors gratefully acknowledge the financial support provided by the National Science and Technology Council (Grant No. NSTC-112-2221-E-131-021, 112-2622-E-131-006, 112-2628-E-131-001-MY4, 113-2221-E-131-021-MY3). The corresponding authors also wish to extend their gratitude for the funding from Chang Gung University, Taiwan (URRPD2N0001). Furthermore, the corresponding author (S.-W. Liu) appreciates Mr. Hsueh-Hsien Wu of Syskey Technology Co., Ltd. (Taiwan) for his invaluable assistance in designing the perovskite fabrication chambers. Special thanks are also to MA-tek Inc. for assisting with SEM characterization.

Appendix A. Supplementary data

Supplementary data to this article can be found online at https://doi.org/10.1016/j.solener.2024.112872.

References

[1] M.D. Bastiani, V. Larini, R. Montecucco, G. Grancini, The levelized cost of electricity from perovskite photovoltaics, Energy Environ. Sci. 16 (2023) 421–429, https://doi.org/10.1039/d2ee03136a.

[2] C. Chen, J. Chen, H. Han, L. Chao, J. Hu, T. Niu, H. Dong, S. Yang, Y. Xia, Y. Chen, W. Huang, Perovskite solar cells based on screen-printed thin films, Nature 612 (2022) 266–271, https://doi.org/10.1038/s41586-022-05346-0.

[3] T. Bu, L.K. Ono, J. Li, J. Su, G. Tong, W. Zhang, Y. Liu, J. Zhang, J. Chang, F. Said Kazaoui, Y.-B. Huang, Y.Q. Cheng, Modulating crystal growth of formamidinium–caesium perovskites for over 200 cm2 photovoltaic sub-modules, Nature Energy. 7 (2022) 528–536, https://doi.org/10.1038/s41560-022-01039-0.

[4] H. Min, D.Y. Lee, J. Kim, G. Kim, K.S. Lee, J. Kim, M.J. Paik, Y.K. Kim, K.S. Kim, M. G. Kim, T.J. Shin, S. Il Seok, Perovskite solar cells with atomically coherent interlayers on SnO2 electrodes, Nature 598 (2021) 444–450, https://doi.org/10.1038/s41586-021-03964-8.

[5] Y. Zhao, F. Ma, Z. Qu, S. Yu, T. Shen, H.-X. Deng, X. Chu, X. Peng, Y. Yuan, X. Zhang, J. You, Inactive (PbI 2) 2 RbCl stabilizes perovskite films for efficient solar cells, Science 377 (2022) 531–534, https://doi.org/10.1126/science.abp8873.

[6] N.-G. Park, K. Zhu, Scalable fabrication and coating methods for perovskite solar cells and solar modules, Nat. Rev. Mater. (2020), https://doi.org/10.1038/s41578-019-0176-2.

[7] Y. Vaynzof, The future of perovskite photovoltaics—thermal evaporation or solution processing? Adv. Energy Mater. 10 (2020) 2003073 https://doi.org/10.1002/aenm.202003073.

[8] T. Abzieher, D.T. Moore, M. Roß, S. Albrecht, J. Silvia, H. Tan, Q. Jeangros, C. Ballif, B.-S. Maximilian Hoerantner, H.J. Kim, P.P. Bolink, J.C. Goldschmidt, Y.-H. Chiang, S.D. Stranks, J. Borchert, M.D. McGehee, M. Morales-Masis, J. Patel, A. Bruno, Vapor phase deposition of perovskite photovoltaics: short track to commercialization? Energy Environ. Sci. 17 (2024) 1645–1663, https://doi.org/10.1039/d3ee03273f.

[9] C. Momblona, L. Gil-Escrig, E. Bandiello, E.M. Hutter, M. Sessolo, K. Lederer, J. Blochwitz-Nimoth, H.J. Bolink, Efficient vacuum deposited p-i-n and n-i-p perovskite solar cells employing doped charge transport layers, Energy Environ. Sci. 9 (2016) 3456–3463, https://doi.org/10.1039/c6ee02100j.

[10] Y. Chiang, K. Frohna, H. Salway, A. Abfalterer, L. Pan, B. Roose, M. Anaya, S. D. Stranks, Vacuum-deposited wide-bandgap perovskite for all-perovskite tandem solar cells, ACS Energy Lett. 8 (2023) 2728–2737, https://doi.org/10.1021/acsenergylett.3c00564.

[11] T. Lei, F. Li, X. Zhu, H. Dong, Z. Niu, S. Ye, W. Zhao, J. Xi, B. Jiao, L. Ding, Z. Wu, Flexible perovskite solar modules with functional layers fully vacuum deposited, Sol. RRL. 4 (2020), https://doi.org/10.1002/solr.202000292.

[12] C. Lidón Gil-Escrig, F.P. Dreessen, E. Zafer Hawash, S. Moons, M. Albrecht, H.J. B. Sessolo, Efficient wide-bandgap mixed-cation and mixed-halide perovskite solar cells by vacuum deposition, ACS Energy Lett. 6 (2021) 827–836, https://doi.org/10.1021/acsenergylett.0c02445.

[13] I. Susic, F. Lidón Gil-Escrig, M. Palazon, H.J.B. Sessolo, Quadruple-cation wide-bandgap perovskite solar cells with enhanced thermal stability enabled by vacuum deposition, ACS Energy Lett. 7 (2022) 1355–1363, https://doi.org/10.1021/acsenergylett.2c00304.

[14] J. Feng, Y. Jiao, H. Wang, X. Zhu, Y. Sun, M. Du, Y. Cao, D. Yang, S.F. Liu, High-throughput large-area vacuum deposition for high-performance formamidine-based perovskite solar cells, Energy Environ. Sci. 14 (2021) 3035–3043, https://doi.org/10.1039/d1ee00634g.

[15] D. Lin, Y. Gao, T. Zhang, Z. Zhan, N. Pang, Z. Wu, K. Chen, T. Shi, Z. Pan, P. Liu, W. Xie, Vapor deposited pure α-FAPbI$_3$ perovskite solar cell via moisture-induced phase transition strategy, Adv. Funct. Mater. 32 (2022), https://doi.org/10.1002/adfm.202208392.

[16] H. Li, J. Zhou, L. Tan, M. Li, C. Jiang, S. Wang, X. Zhao, Y. Liu, Y. Zhang, Y. Ye, W. Tress, C. Yi, Sequential vacuum-evaporated perovskite solar cells with more than 24% efficiency, Sci. Adv. 8 (2022), https://doi.org/10.1126/sciadv.abo7422.

[17] F.M. Rombach, S.A. Haque, T.J. Macdonald, Lessons learned from spiro-OMeTAD and PTAA in perovskite solar cells, Energy Environ. Sci. 14 (2021) 5161–5190, https://doi.org/10.1039/d1ee02095a.

[18] D.B. Ritzer, T. Abzieher, A. Basibüyük, T. Feeney, F. Laufer, S. Ternes, B. S. Richards, S. Bergfeld, U.W. Paetzold, Upscaling of perovskite solar modules: The synergy of fully evaporated layer fabrication and all-laser-scribed interconnections, Prog. Photovoltaics Res. Appl. 30 (2021) 360–373, https://doi.org/10.1002/pip.3489.

[19] I. Susic, A. Kama, L. Gil-Escrig, C. Dreessen, F. Palazon, D. Cahen, M. Sessolo, H. J. Bolink, Combinatorial vacuum-deposition of wide bandgap perovskite films and solar cells, Adv. Mater. Interfaces 10 (2022), https://doi.org/10.1002/admi.202202271.

[20] Z. Liu, X. Wang, H. Ge, A. Li, X.-F. Wang, Recent research progress and perspectives on porphyrin and phthalocyanine analogues for perovskite solar cell applications, Energy Fuels (2024), https://doi.org/10.1021/acs.energyfuels.4c02136.

[21] M.M. Tavakoli, P. Yadav, D. Prochowicz, R. Tavakoli, Efficient, hysteresis-free, and flexible inverted perovskite solar cells using all-vacuum processing, Sol. RRL 5 (2020) 2000552, https://doi.org/10.1002/solr.202000552.

[22] Q. Yuan, K.B. Lohmann, R.D.J. Oliver, A.J. Ramadan, S. Yan, J.M. Ball, M. Greyson Christoforo, N.K. Noel, H.J. Snaith, L.M. Herz, M.B. Johnston, Thermally stable perovskite solar cells by all-vacuum deposition, ACS Appl. Mater. Interfaces 15 (2022) 772–781, https://doi.org/10.1021/acsami.2c14658.

[23] S. Yuan, K. Mao, F. Cai, Z. Zhu, H. Meng, T. Li, W. Peng, X. Feng, W. Chen, J. Xu, J. Xu, Understanding and engineering the perovskite/organometallic hole transport interface for high-performance p–i–n single cells and textured tandem solar cells, ACS Energy Letters 3557–3566 (2024), https://doi.org/10.1021/acsenergylett.4c01301.

[24] T. Abzieher, T. Feeney, F. Schackmar, Y.J. Donie, I.M. Hossain, J.A. Schwenzer, T. Hellmann, T. Mayer, M. Powalla, U.W. Paetzold, From groundwork to efficient solar cells: on the importance of the substrate material in co-evaporated perovskite solar cells, Adv. Funct. Mater. 31 (2021), https://doi.org/10.1002/adfm.202104482.

[25] H. Zhu, S. Teale, M.N. Lintangpradipto, S. Mahesh, B. Chen, M.D. McGehee, E. H. Sargent, O.M. Bakr, Long-term operating stability in perovskite photovoltaics, Nat. Rev. Mater. 8 (2023) 569–586, https://doi.org/10.1038/s41578-023-00582-w.

[26] Y.-H. Chiang, M. Anaya, S.D. Stranks, Multisource vacuum deposition of methylammonium-free perovskite solar cells, ACS Energy Lett. 5 (2020) 2498–2504, https://doi.org/10.1021/acsenergylett.0c00839.

[27] M.-G. La-Placa, D. Lidón Gil-Escrig, F. Guo, T.J. Palazón, M. Savenije, H.J. B. Sessolo, Vacuum-deposited 2D/3D Perovskite heterojunctions, ACS Energy Lett. 4 (2019) 2893–2901, https://doi.org/10.1021/acsenergylett.9b02224.

[28] Z.-W. Gao, Y. Wang, W. Choy, Buried interface modification in perovskite solar cells: A materials perspective, Adv. Energy Mater. 12 (2022) 2104030, https://doi.org/10.1002/aenm.202104030.

[29] A. Amin, C.-C. Lee, Y.-C. Huang, C.-J. Shih, R. Estrada, M.-H. Sajal Biring, C.-F. Kuo, Y.-C. Li, S.-W. Huang, Achieving a highly stable perovskite photodetector with a long lifetime fabricated via an all-vacuum deposition process, ACS Appl. Mater. Interfaces 15 (2023) 21284–21295, https://doi.org/10.1021/acsami.3c00839.

[30] J. Ibaceta-Jaña, R. Muydinov, P. Rosado, H. Mirhosseini, M. Chugh, O. Nazarenko, D.N. Dirin, D. Heinrich, M.R. Wagner, T.D. Kühne, B. Szyszka, M.V. Kovalenko, A. Hoffmann, Vibrational dynamics in lead halide hybrid perovskites investigated by Raman spectroscopy, Phys. Chem. Chem. Phys. 22 (2020) 5604–5614, https://doi.org/10.1039/c9cp06568g.

[31] J. Yan, J. Zhao, H. Wang, L.J. Mels Kerklaan, B. Bannenberg, T.J. Ibrahim, L. Savenije, O.I. Mazzarella, Crystallization process for high-quality $Cs_{0.15}FA_{0.85}PbI_{2.85}Br_{0.1}5$ film deposited via simplified sequential vacuum evaporation, ACS Appl. Energy Mater. 6 (2023) 10265–10273, https://doi.org/10.1021/acsaem.3c00203.

[32] R. Ji, Z. Zhang, C. Cho, Q. An, F. Paulus, M. Kroll, M. Löffler, F. Nehm, B. Rellinghaus, K. Leo, Y. Vaynzof, Thermally evaporated methylammonium-free perovskite solar cells, J. Mater. Chem. C 8 (2020) 7725–7733, https://doi.org/10.1039/D0TC01550D.

[33] S. Haque, M.J. Mendes, H. Olalla Sanchez-Sobrado, E. Águas, R.M. Fortunato, Photonic-structured TiO2 for high-efficiency, flexible and stable Perovskite solar cells, Nano Energy 59 (2019) 91–101, https://doi.org/10.1016/j.nanoen.2019.02.023.

[34] W. Tress, N. Marinova, O. Inganäs, M.K. Nazeeruddin, S.M. Zakeeruddin, M. Grätzel, Predicting the open-circuit voltage of $CH_3NH_3PbI_3$ perovskite solar cells using electroluminescence and photovoltaic quantum efficiency spectra: the role of radiative and non-radiative recombination, Adv. Energy Mater. 5 (2015) 1400812, https://doi.org/10.1002/aenm.201400812.

[35] C. Dong, D. Liu, A. Zhang, X. Yang, H. Song, L. Hu, X. Li, L. Xu, L. Wang, C. Chen, J. Tang, Co-evaporated oriented DMA1-Cs PbI3 perovskite films for photovoltaics, Nano Energy 120 (2024) 109159, https://doi.org/10.1016/j.nanoen.2023.109159.

[36] C. Eames, J.M. Frost, P.R.F. Barnes, B.C. O'Regan, A. Walsh, M.S. Islam, Ionic transport in hybrid lead iodide perovskite solar cells, Nat. Commun. 6 (2015), https://doi.org/10.1038/ncomms8497.

[37] H. Back, G. Kim, J. Kim, J. Kong, T.K. Kim, H. Kang, H. Kim, J. Lee, S. Lee, K. Lee, Achieving long-term stable perovskite solar cells via ion neutralization, Energy Environ. Sci. 9 (2016) 1258–1263, https://doi.org/10.1039/C6EE00612D.

[38] Z. Huang, A.H. Proppe, H. Tan, M.I. Saidaminov, F. Tan, A. Mei, C.-S. Tan, M. Wei, Y. Hou, H. Han, S.O. Kelley, E.H. Sargent, Suppressed ion migration in reduced-dimensional perovskites improves operating stability, ACS Energy Lett. 4 (2019) 1521–1527, https://doi.org/10.1021/acsenergylett.9b00892.

[39] M.V. Khenkin, E.A. Katz, A. Abate, G. Bardizza, J.J. Berry, C. Brabec, F. Brunetti, V. Bulović, Q. Burlingame, A. Di Carlo, R. Cheacharoen, Y.-B. Cheng, A. Colsmann, S. Cros, K. Domanski, M. Dusza, C.J. Fell, S.R. Forrest, Y. Galagan, D. Di Girolamo, Consensus statement for stability assessment and reporting for perovskite photovoltaics based on ISOS procedures, Nat. Energy 5 (2020) 35–49, https://doi.org/10.1038/s41560-019-0529-5.

[40] K. Domanski, B. Roose, T. Matsui, M. Saliba, S.-H. Turren-Cruz, J.-P. Correa-Baena, C.R. Carmona, G. Richardson, J.M. Foster, F. De Angelis, J.M. Ball, A. Petrozza, N. Mine, M.K. Nazeeruddin, W. Tress, M. Grätzel, U. Steiner, A. Hagfeldt, A. Abate, Migration of cations induces reversible performance losses over day/night cycling in perovskite solar cells, Energy Environ. Sci. 10 (2017) 604–613, https://doi.org/10.1039/c6ee03352k.

[41] J.A. Christians, P. Schulz, J.S. Tinkham, T.H. Schloemer, S.P. Harvey, B.J. Tremolet de Villers, A. Sellinger, J.J. Berry, J.M. Luther, Tailored interfaces of unencapsulated perovskite solar cells for >1,000 hour operational stability, Nat. Energy 3 (2018) 68–74, https://doi.org/10.1038/s41560-017-0067-y.

[42] L. Gil-Escrig, C. Dreessen, I.C. Kaya, B.-S. Kim, F. Palazon, M. Sessolo, H.J. Bolink, Efficient vacuum-deposited perovskite solar cells with stable cubic $FA_{1-x}MA_xPbI_3$, ACS Energy Lett. 5 (2020) 3053–3061, https://doi.org/10.1021/acsenergylett.0c01473.

[43] D. Luo, R. Su, W. Zhang, Q. Gong, R. Zhu, Minimizing non-radiative recombination losses in perovskite solar cells, Nat. Rev. Mater. 5 (2019) 44–60, https://doi.org/10.1038/s41578-019-0151-y.

[44] O. Almora, C.I. Cabrera, J. Garcia-Cerrillo, T. Kirchartz, U. Rau, C.J. Brabec, Quantifying the absorption onset in the quantum efficiency of emerging photovoltaic devices, Adv. Energy Mater. 11 (2021), https://doi.org/10.1002/aenm.202100022.
[45] T. Kirchartz, J.A. Marquez, M. Stolterfoht, T. Unold, Photoluminescence-based characterization of halide perovskites for photovoltaics, Adv. Energy Mater. 10 (2020), https://doi.org/10.1002/aenm.201904134.
[46] N. Klipfel, C. Momblona, H. Kanda, N. Shibayama, Y. Nakamura, M.D. Mensi, C. Liu, C. Roldán-Carmona, M.K. Nazeeruddin, Crystallographically oriented hybrid perovskites via thermal vacuum codeposition, Sol. RRL. 5 (2021), https://doi.org/10.1002/solr.202100191.
[47] E. Regalado-Pérez, E.B. Díaz-Cruz, J. Landa-Bautista, N.R. Mathews, X. Mathew, Impact of vertical inhomogeneity on the charge extraction in perovskite solar cells: A study by depth-dependent photoluminescence, ACS Appl. Mater. Interfaces 13 (2021) 11833–11844, https://doi.org/10.1021/acsami.0c20826.
[48] H. Xu, Y. Wu, J. Cui, C. Ni, F. Xu, J. Cai, F. Hong, Z. Fang, W. Wang, J. Zhu, L. Wang, R. Xu, F. Xu, Formation and evolution of the unexpected PbI_2 phase at the interface during the growth of evaporated perovskite films, Phys. Chem. Chem. Phys. 18 (2016) 18607–18613, https://doi.org/10.1039/c6cp02737g.
[49] S. Olthof, K. Meerholz, Substrate-dependent electronic structure and film formation of MAPbI3 perovskites, Sci. Rep. 7 (2017), https://doi.org/10.1038/srep40267.
[50] J. Yan, Lena Sophie Stickel, van, H. Wang, Prasaanth Ravi Anusuyadevi, Agnieszka Kooijman, X. Liu, B. Ibrahim, J.M.C. Mol, P. Taheri, L. Mazzarella, O. Isabella, T.J. Savenije, Vacuum Deposited Perovskites with a Controllable Crystal Orientation, J. Phys. Chem. Lett. 14 (2023) 8787–8795. https://doi.org/10.1021/acs.jpclett.3c01920.
[51] M. Xiao, T. Lu, T. Lin, J.S. Andre, Z. Chen, Understanding molecular structures of buried interfaces in halide perovskite photovoltaic devices nondestructively with sub-monolayer sensitivity using sum frequency generation vibrational spectroscopy, Adv. Energy Mater. 10 (2019) 1903053, https://doi.org/10.1002/aenm.201903053.
[52] X. Yang, D. Luo, Y. Xiang, L. Zhao, M. Anaya, Y. Shen, J. Wu, W. Yang, Y.-H. Chiang, Y. Tu, R. Su, Q. Hu, H. Yu, G. Shao, W. Huang, T.P. Russell, Q. Gong, S. D. Stranks, W. Zhang, R. Zhu, Buried interfaces in halide perovskite photovoltaics, Adv. Sci. 33 (2021) 2006435, https://doi.org/10.1002/adma.202006435.
[53] C. Zhu, X. Niu, Y. Fu, N. Li, C. Hu, Y. Chen, X. He, G. Na, P. Liu, H. Zai, Y. Ge, Y. Lu, X. Ke, Y. Bai, S. Yang, P. Chen, Y. Li, M. Sui, L. Zhang, H. Zhou, Strain engineering in perovskite solar cells and its impacts on carrier dynamics, Nat. Commun. 10 (2019), https://doi.org/10.1038/s41467-019-08507-4.
[54] J. Patel, J. Wong-Leung, N. Stephan van Reenen, J.E. Sakai, E.S. Wang, M. Parrott, H.J. Liu, L.M. Snaith, M.V.J. Herz, Influence of interface morphology on hysteresis in vapor-deposited perovskite solar cells, Adv. Electron. Mater. 3 (2017) 1600470, https://doi.org/10.1002/aelm.201600470.
[55] X. Li, W. Wang, P. Huang, L. Yang, J. Hu, K. Wei, L. Gao, Y. Jiang, K. Sun, G. Du, X. Cai, C. Liu, W. Tang, J. Zhang, Fluorinated naphthalene diimides as buried electron transport materials achieve over 23% efficient perovskite solar cells, Adv. Sci. (2024), https://doi.org/10.1002/advs.202403735.
[56] G. Wang, W. Duan, Q. Lian, M.A. Mahmud, T.L. Leung, C. Liao, J. Bing, C. Bailey, J. Yi, R. Tao, J. Yang, X. Cui, S. Nie, Y. Zhu, A. Lambertz, M. Jankovec, M. Topič, D. R. McCamey, S. Bremner, Z. Hameiri, Reducing voltage loss via dipole tuning for electron-transport in efficient and stable perovskite-silicon tandem solar cells, Adv. Energy Mater. (2024), https://doi.org/10.1002/aenm.202401029.
[57] B. Jiang, Z. Gao, C. Lung, Z. Shi, H. Du, Y. Su, H. Shih, K. Lee, H. Hung, C.K. Chan, C. Chen, K. Wong, Enhancing the efficiency of indoor perovskite solar cells through surface defect passivation with coplanar heteroacene cored A-D–A-type molecules, Adv. Funct. Mater. (2023), https://doi.org/10.1002/adfm.202312819.